

Supporting Information for:

Quantitative multicolor subdiffraction imaging of bacterial protein ultrastructures in 3D

*Andreas Gahlmann^a, Jerod L. Ptacin^c, Ginni Grover^b, Sean Quirin^b,
Alexander R. S. von Diezmann^a, Marissa K. Lee^a, Mikael P. Backlund^a,
Lucy Shapiro^c, Rafael Piestun^b, and W. E. Moerner^a*

^aDepartment of Chemistry, Stanford University, Stanford, CA 94305

^bDepartment of Electrical, Computer, and Energy Engineering, University of Colorado at
Boulder, 425 UCB, Boulder, CO 80309

^cDepartment of Developmental Biology, Stanford University School of Medicine, Beckman
Center, Stanford, CA 94305

Table of Contents

1	Phase masks.....	3
2	Optical Setup	4
3	Localization precision calibration	5
4	Fiducial calibration	6
5	3D Image Registration.....	6
6	Contributors to the non-zero registration error.....	8
7	Construction of bacterial strains	10
8	Sample preparation	12
9	Single-molecule imaging of doubly-labeled strains	12
10	Image analysis including wavelet estimation of background	13
11	Measurements on CreS fibers	14
12	PopZ Volume Estimation.....	15
13	Supplementary Figures	17
14	Supplementary Online Videos	23
15	References.....	25

1 Phase masks

The DH-PSF phase masks used in each of the two channels were fabricated by a multi-step optical lithography process. The phase mask design has vortex singularities at particular positions along with phase gradients throughout the mask³⁶. As reported earlier, one method for phase mask fabrication utilizes a grayscale photolithographic process¹⁸. A second method of phase mask fabrication uses a sequence of binary lithographic steps to convert a phase gradient into a multi-step height relief³⁷⁻³⁹. The advantage of this method is its high repeatability. Each phase mask reported here is an 8-level surface relief pattern with surface height $h = \lambda\varphi \left[2\pi(n(\lambda) - 1) \right]$, where λ is the operating wavelength, $n(\lambda)$ is the wavelength dependent refractive index of the mask material and φ is the amount of phase retardation imposed by the DH-PSF mask. Converting the gradient phase to a quantized 8-level step phase pattern produced only a slight effect on the DH-PSF behavior. The efficiency, defined as the fraction of energy residing in the two main lobes of the DH-PSF, is reduced by 3% from the efficiency of the original design of 57%³⁶.

The process of mask fabrication started with a clean quartz slide (Electron Microscopy Sciences, Part no. 72250-01, 1 mm thick) upon which we sputtered an optically opaque layer of chrome that was subsequently processed into a circular aperture window with a diameter of 2.7 mm. After a layer of positive photoresist (Clariant AZ-4210) was spin-coated over the chrome, the quartz slide was aligned to a binary mask with a clear aperture (diameter = 2.7 mm) using a SUSS MJB4 mask aligner and the resist was then exposed (Heidelberg DWL 66FS). The resist was developed in Clariant AZ400K developer (1:4 ratio with DI water) to remove the exposed photoresist and the chrome was later removed by wet etching (using CR-8 chrome

etchant) to create the clear aperture. The remaining photoresist was stripped away with a sonicating bath of Clariant AZ-400T.

As described in Ref. 38, M suitably designed binary masks can be used in sequence to create 2^M discrete heights. For the phase masks used here, $M = 3$ and the design of each binary mask follows from first digitally approximating the exact, continuous mask as an 8-level mask and then following the algorithms in Ref. 38 to design the appropriate three binary masks. The process of transferring these binary patterns into a surface relief of quartz was as follows. On the quartz slide, the side opposite of the chrome coat was spin-coated with AZ-4210 photoresist to produce a $\sim 2 \mu\text{m}$ layer. The quartz slide was aligned with the first of three binary masks using the SUSS MJB4 mask aligner and then exposed. The photo-resist was developed and removed to expose a layer of quartz. The quartz was then etched using Reactive Ion Etching (RIE) (STS ICP Etcher) to remove half of the maximum surface relief height. The remaining AZ-4210 photoresist was stripped using a sonicating bath of AZ-400T. This sequence, beginning with spin-coating another layer of AZ-4210 photoresist, was repeated with the second and then the third masks to remove $1/4$ and $1/8$ the maximum surface relief height, respectively. After the third RIE treatment, the 8-level surface had been transferred into the quartz and the chrome window on the opposite side serves as the limiting aperture. The surface-reliefs of the phase masks were measured using a white-light interferometer (Zygo, New-view) and are shown in Supplementary Figure 1ab.

2 Optical Setup

The dual channel DH-PSF microscope consists of an inverted fluorescence microscope stand (Nikon Diaphot 200) with only the internal tube lens removed. Fluorescence from the sample is

collected by a high NA oil-immersion objective (Olympus UPlanSApo 100X/1.40NA) and filtered through a dual pass dichroic mirror (Chroma, zt440/514/561rpc). The intermediate image is produced by an externally placed tube lens outside of the microscope stand. Given the numerical aperture of the microscope objective, the focal lengths of the tube lens ($f = 225$ mm) and the $4f$ lenses ($f = 120$ mm) are chosen to match the size of the demagnified objective lens pupil to the size of the phase masks (diameter = 2.7 mm). Fluorescence is further filtered in front of the 560 nm dichroic beamsplitter (Semrock, FF560-FDi01) with a 514 nm long pass filter (Semrock, LP02-514RE) and a 561 nm notch filter (Semrock, NF03-561E). The fluorescence directed into the red channel is further filtered with a 610 ± 30 nm bandpass filter (Semrock, FF01-523/610) to reduce the autofluorescence background of the glass slides excited with the 514 nm excitation laser. After phase modulation by the phase masks, the fluorescence in each channel is imaged onto a separate region of an electron-multiplying charge coupled camera (Andor Ixon DU-897E).

3 Localization precision calibration

To determine the statistical localization precision of a single molecule in the x , y , and z dimensions for different integrated signal photon counts and background photon counts, we repeatedly imaged and localized stationary fluorescent beads (Molecular Probes, 540/560 carboxylate-modified FluoSpheres, 100 nm diameter) immobilized in a PVA polymer film. We chose an integration time of 6 ms and acquired 1000 frames. During the 6 seconds of total acquisition time, the microscope setup did not produce any measurable drift and the beads did not photobleach substantially. To produce the desired number of fluorescent photons on the detector, we adjusted the power of the imaging laser. To produce the desired number of

background photons on the detector, we adjusted the intensity from a white-light halogen source illuminating the sample from above. We ensured that this artificially created background was spatially uniform throughout the 64×64 pixel image. The beads were positioned such that their DH-PSF image appeared on one side of the 64×64 pixel image. In this way the signal and the background levels, as well as the 3D positions of the bead could be directly measured in each frame. The obtained quantities were then averaged throughout the 1000 frame image stack. The standard deviation of the 1000 position measurements produced the final statistical localization precision in x , y , and z shown in Figure 2ab.

4 Fiducial calibration

Single-molecule positions are extracted relative to the position of a fiducial bead. We calibrated the DH-PSF angle, midpoints, and statistical localization precision as a function of z defocus by stepping the microscope objective relative to the fiducial bead in 50 nm increments using a piezoelectric objective scanner (Mad City Labs, C-focus)¹². Any apparent motion of the bead in x , y due to tilt and estimator inaccuracy is thus calibrated in this procedure and is subsequently removed from single-molecule position determinations. This calibration step also produces template images of the DH-PSF which are used for the identification of single-molecule signals during postprocessing of the raw data.

5 3D Image Registration

The array of control point positions was generated by using the DH-PSF and double-Gaussian fitting to extract x , y , and z positions for ~ 15 fluorescent beads in a $30 \times 30 \mu\text{m}$ image, translating the sample in z by 200-300 nm through a $1.5 \mu\text{m}$ range, then translating the sample in x and y to

obtain ~15 new bead positions, and repeating this procedure multiple times. The effect of this procedure is to stochastically sample the 3D image domain at a very fine scale, using only the fact that, for any one image, the beads represent static markers that are simultaneously detectable in both color channels. Thus, precise control over the translations of the sample is not required.

The mapping function \mathbf{t} transforms points from one coordinate system into another⁴⁰

$$\mathbf{x} \xrightarrow{\mathbf{t}(\mathbf{x})} (\mathbf{x}').$$

For coordinate transformations in 3-dimensional space, $\mathbf{t}(\mathbf{x})$ has three components $t_{x'}$, $t_{y'}$, and $t_{z'}$, that separately estimate the three coordinates x' , y' , and z' ,

$$\mathbf{t}(\mathbf{x}) = (t_{x'}(x, y, z), t_{y'}(x, y, z), t_{z'}(x, y, z)) = (x', y', z').$$

The component functions $t_{x'}$ are given as the weighted mean of polynomial transformations $L_{i,x'}$ using the local weights W_i associated with the i^{th} control point with coordinates \mathbf{x}_i ,

$$t_{x'}(\mathbf{x}) = \frac{\sum_{i=1}^N L_{i,x'}(\mathbf{x}) W_i(\mathbf{x})}{\sum_{i=1}^N W_i(\mathbf{x})},$$

where the sum is over the full set of N control points in the image domain.

The polynomial transformation functions are defined to evaluate to the coordinates \mathbf{x}' , if $\mathbf{x} = \mathbf{x}_i$, so that corresponding control points are directly mapped. The 3D linear transformation is given by

$$\begin{aligned} L_{i,x'}(x, y, z) &= a_{i,x'}(x - x_i) + b_{i,x'}(y - y_i) + c_{i,x'}(z - z_i) + x' \\ L_{i,y'}(x, y, z) &= a_{i,y'}(x - x_i) + b_{i,y'}(y - y_i) + c_{i,y'}(z - z_i) + y' \\ L_{i,z'}(x, y, z) &= a_{i,z'}(x - x_i) + b_{i,z'}(y - y_i) + c_{i,z'}(z - z_i) + z' \end{aligned}$$

For a 3D quadratic transformation the x' component is given by

$$\begin{aligned}
L_{i,x'}(x, y, z) = & a_{i,x'}(x - x_i)^2 + b_{i,x'}(y - y_i)^2 + c_{i,x'}(z - z_i)^2 \\
& + d_{i,x'}(x - x_i)(y - y_i) + e_{i,x'}(x - x_i)(z - z_i) + f_{i,x'}(y - y_i)(z - z_i) \\
& + g_{i,x'}(x - x_i) + h_{i,x'}(y - y_i) + i_{i,x'}(z - z_i) + x'
\end{aligned}$$

and the y' and z' components are similarly defined. For our datasets, we determined that quadratic polynomials gave satisfactory results, while keeping computational cost at a reasonable level. If needed, however, higher-order polynomials can be utilized in a straightforward manner.

The weight associated with the i^{th} control point is given as a 3D Gaussian sphere centered at \mathbf{x}_i

$$W_i(\mathbf{x}) = \exp \left\{ -\frac{(x - x_i)^2 + (y - y_i)^2 + (z - z_i)^2}{2(s\sigma_i)^2} \right\}.$$

For the automated computation of the complete transformation function, the user needs to specify three parameters, namely the number of neighboring control points n used to calculate the coefficients of the polynomial transformation by least-squares estimation and parameters s and σ_i that define the spatial extent of the Gaussian weighting functions. These three parameters are systematically determined for each set of control points to produce the lowest overall registration errors. Here, we obtained the best results with $n = 46$, $s = 0.9$, and σ_i as being equal to the Euclidian distance to the 7th closest control point. Defining σ_i in this way guarantees that the size of the weights is automatically adjusted to account for changes in local control point densities and that $\mathbf{t}(\mathbf{x})$ is always defined over the entire image domain.

6 Contributors to the non-zero registration error

In previous work, registration errors based on a locally-weighted transformation function in 2D were in the range of 5-15 nm^{27, 43}. We can safely rule out the localization precision as major

contributor, because the standard errors of the mean bead positions are about a factor of 5-10 smaller than the obtained registration errors. The standard errors are computed as $\sigma_{x,y,z}/\sqrt{m}$, where $m = 8$ is the number of times the bead were imaged and localized and $\sigma_{x,y,z}$ are the respective standard deviations of these m measurements.

The localization accuracy, on the other hand, is limited by two different instrumental effects. First, it is possible that the optical response function of the DH-PSF microscope will drift over time, e.g. due to temperature fluctuation in the laboratory and the resulting nanoscale movements of the optical mounts. The acquisition of a dataset yielding <4000 control point localizations takes about 10 minutes. However, since the resulting mapping function will be used to register and fuse imaging data acquired that same day, these movements need to be minimized over a period of at least several hours. We repeated our calibrations of the DH-PSF response (see Fiducial calibration) over the course of a 5 hour period (Supplementary Figure 2ab). In our setup, these calibrations revealed a drift in the optical response function that is of the same magnitude as the obtained registration errors, i.e. ± 8 nm in x,y and z .

Second, the localization accuracy can be systematically affected by the interpixel photoresponse non-uniformity (PRNU) of the wide-field EM-CCD detector. The PRNU effect has been shown in a different 2D setup to limit the localization accuracy to several nanometers when a very small field-of-view is considered⁴⁴. In this study, we sample the entire field of view and, consequently, the mean nearest neighbor distance for our sets of control points is ~ 150 nm, but only because we finely sample the z dimension. In the x and y dimension the control points are separated by $\sim 1-2$ μm . These sampling intervals are much larger than the sub-pixel intervals that are required to accurately quantify the PRNU and remove its associated effect on the localization accuracy. Because in this work the coefficients of the polynomial mapping

functions are determined in a least-squares sense using the nearest 46 control point locations, this systematic error was left unaccounted for and was therefore propagated into the FRE and TRE values.

The final contributor to the registration error is the finite density of control points. To quantify this effect we repeated our control point measurements to even further increase the number of control points per volume. Limiting our investigations to a smaller $18 \times 18 \times 0.7 \mu\text{m}$ volume containing $N = 6004$ control points near the center of the field of view, we repeatedly and randomly selected a fractional subset of control points and calculated the associated FRE and TRE values. Indeed, we were able to lower the mean TRE to 5.84 nm using the full set of control points, but even with this (higher) density of control points, we did not achieve an asymptotic limit (Supplementary Figure 2c). It is clear from previous work⁴⁴ that (in the absence of instrumental drift) an ever increasing density of control points will eventually lead to sub-pixel sampling of the field-of-view and produce sub-nanometer TRE values, because, in such a case, the PRNU effect of the detector will be directly calibrated. It is important to note, however, that sub-pixel sampling of the entire 3D field-of-view of the DH-PSF microscope would be prohibitively time-consuming.

7 Construction of bacterial strains

To enable two-color super-resolution imaging of both PopZ and CreS structures in *Caulobacter*, we created strains that expressed eYFP- or PAmCherry1-tagged CreS and PopZ fusions in the wild type *Caulobacter* CB15N background. The strain JP431 contains a xylose-inducible *creS-eyfp* fusion integrated at the chromosomal *xylX* locus and a vanillic acid-inducible *creS-PAmCherry1* gene integrated at the *vanA* locus in the *Caulobacter* chromosome. To

generate this strain, the *PAmCherry1* gene was PCR amplified from the plasmid PAmCherry1-N1 (Clontech) using the primers 5'CGCGTCACCGGTCGGCCACCATGGTGAGCAAGGGCGAGGAGGATAACATG and 5'GACATAGCTAGCTTACTTGTACAGCTCGTCCATGCCGCCGGTG. The resulting PCR product was digested with AgeI and NheI and cloned into the AgeI/NheI sites in the plasmid pVYFPC-2⁴¹ to generate the plasmid pJP363 (pVPAmCherry1C2). Next, the plasmid pJP124¹³ was digested with NdeI and SacI, and the resulting *creS* fragment was cloned into the NdeI and SacI sites of pJP363 to generate the plasmid pJP387 (pVPAmCherry1C2-creS). This plasmid (pJP387) was electroporated into the *Caulobacter* strain JP198¹³ to generate JP431.

The strain JP432 contains a xylose-inducible *pAmCherry1-popZ* gene fusion integrated at the chromosomal *xylX* locus and a vanillic acid-inducible *creS-eyfp* gene fusion integrated at the chromosomal *vanA* locus. To generate JP432, the *popZ* gene was released from the plasmid pJP44³² using KpnI and EcoRI and was cloned into the KpnI and EcoRI sites in the plasmid pXCHYN-2⁴¹ to create the plasmid pJP320 (pXCHYN2-popZ). Next, the *PAmCherry1* gene was amplified from the plasmid PAmCherry1-N1 (Clontech) using the primers 5'GCATCACATATGGTGAGCAAGGGCGAGGAGGATAACATG and 5'CTTAAGGTACATGCATATTAATTAAGGCGCCTGCAGGCTTGTACAGCTCGTCCATGCCGCCGGTGGAGTG, which added a 5' NdeI and 3' KpnI site. This PCR product was digested with NdeI and KpnI and cloned into these sites on the plasmid pJP320 to create the plasmid pJP341 (pXPAmCherry1N2-popZ). This plasmid (pJP341) was electroporated into wild type *Caulobacter* CB15N and integrated into the *xylX* locus of the chromosome to create the strain JP350. Next, the *creS* gene was released from the plasmid pJP124¹³ using NdeI and SacI and cloned into the NdeI and SacI sites in the plasmid pVYFPC-5⁴¹ to create the plasmid pJP388

(pVYFPC5-creS). This plasmid (pJP388) was subsequently electroporated into JP350, integrating into the *vanA* locus of the chromosome to create the strain JP432.

8 Sample preparation

For imaging experiments, cultures of *C. crescentus* strains were grown at log phase in minimal growth media (M2G) at 28 °C for 2-3 days. We controlled the expression level of fluorescent protein fusions from their respective inducible promoters by adding inducer to the culture medium for a given amount of time. Strain JP431 was simultaneously induced with 0.06% xylose and 0.1 mM vanillate for 120 min to express CreS-PAmCherry1 and CreS-eYFP, respectively. Strain JP432 was simultaneously induced with 0.06% xylose and 0.1 mM vanillate for 120 min to express PAmCherry1-PopZ and CreS-eYFP, respectively. After the induction period, the bacterial cultures were pelleted three times (8,000 rpm for 3 min) and then resuspended in clean M2G imaging buffer to obtain clean imaging conditions. In the final resuspension step, a small amount of M2G was added to produce a concentrated cell culture. To 40 μ L of this cell culture, we added 1 μ L of fluorescent bead suspension to provide fiducial marks (Molecular Probes, 565/580 carboxylate-modified FluoSpheres, 200 nm diameter, 10000X dilution from stock into M2G). 1 μ L of the final imaging suspension was deposited on an agarose pad (Sigma, 1.5% in M2G) and then mounted on a glass slide (Fisher Finest, No. 1, 35 \times 50 mm) and imaged without delay.

9 Single-molecule imaging of doubly-labeled strains

Imaging of blinking single eYFP molecules was performed with a 514 nm laser beam (Coherent Sapphire 514-100 CW) with a peak intensity of 6.0 kW/cm² and a beam radius of

17 μm ($1/e^2$), similar to the experiment described previously¹³. Single molecules of PAmCherry1 were activated with short pulses (50–100 ms) of low-intensity UV laser light (Coherent, Cube, 403 nm, $<1 \text{ W/cm}^2$) and subsequently imaged with a 561 nm laser beam (Crystalaser, 561 nm) with a peak intensity of 2.0 kW/cm^2 and a beam radius of 19 μm ($1/e^2$). The two-color imaging was interleaved, with reading light toggling between 514 nm (20 frames) and 561 nm (50 frames), for a total imaging time of 13 min for Figure 4cd, for example. Subsequently, PAINT imaging of Nile Red was performed under the same imaging conditions as PAmCherry1, but the activation laser pulses were omitted. Frame integration times of 50 ms were used in all imaging experiments. To introduce the PAINT dye to the imaging environment, we diluted a Nile Red/DMSO stock solution ($0.40 \pm 0.03 \text{ mM}$, determined with a Cary 6000i UV-Vis/NIR Spectrophotometer) 10000 times into M2G imaging buffer. After fluorescent protein imaging was completed, we pipetted 20 μL of that solution to the edge of the agarose pad without moving the sample. Nile red molecules in solution then reached the immobilized bacterial cells by diffusion.

10 Image analysis including wavelet estimation of background

The 3D positions of single molecules were determined with custom software written in MATLAB (MathWorks), as described previously¹³. The precision of each single-molecule localization was determined with Equation 1 using the measured background level and integrated signal photon counts for that molecule. The spatially slowly-varying background due to the wide-field illumination spot was estimated and subtracted in each frame using a custom 2D wavelet filtering algorithm written in MATLAB. Because DH-PSF signals of single molecules are well-localized in both real space and frequency space, the task is well-suited for wavelet-

based analysis. The algorithm works as follows. First, each image was subjected to a 4-level decomposition using the MATLAB built-in function `wavedec2` with third-order Daubechies wavelets and scaling functions. Next, all detail coefficients were set to zero, leaving only approximation coefficients as possibly nonzero. Of the approximation coefficients, those that were larger and smaller than the median value by a chosen amount were recalculated as the local average of the neighboring coefficients. This assured that lower spatial frequency aggregates or the extended intensity around bright fiducial beads were not incorrectly included in the background estimation. Finally, an image was reconstructed from the filtered coefficients and a Gaussian blur function was applied to obtain a smooth estimation of the background.

11 Measurements on CreS fibers

The positions of the labeled CreS molecules in each channel were fit to the parametric equations of a distorted helix with x the position along the helix axis parameterized by t , and y and z defining a point on the helix on a plane perpendicular to the helix axis

$$\begin{aligned}x &= \int_0^t b(t) dt \\y &= r(t) \cos(2\pi t + \phi) \\z &= r(t) \sin(2\pi t + \phi)\end{aligned}$$

where we provide for a slightly distorted helix by allowing the helical slope $b(t) = \frac{dx}{dt}$ and the helical radius $r(t)$ to vary at each point t . With this flexible model function it was possible to find a good fit to the CreS localizations belonging to a given fiber. All fitting was performed using custom scripts written in MATLAB. First the single-molecule localization data was fit to a cylindrical surface to find the central axis of the helix⁴² and the fiber was rotated such that the x axis was collinear with the central axis. Then, to account for distortions of the helix, the slope

$b(t)$ and the radius $r(t)$ were estimated from the rotated dataset (Supplementary Figure 3ef).

Sometimes, the CreS fibers appeared “frayed” at the end, precluding a reliable fit. In these cases, we therefore manually limited the range of the parameter t and only fit the central portions of the fiber.

The width of the CreS fiber was calculated by measuring the perpendicular distances of the individual single-molecule localizations from the fitted helical curve. Because the helices are curved in three dimensions, we defined a thin cylindrical volume centered on the fitted curve and sliding along the range of t to select single-molecule localizations. Within this sliding volume, we define a local coordinate system, x' y' z' , that continually rotates, such that z' is always collinear with the direction of the helix at each point t . The resulting radial distribution histograms in the helix coordinate system can then be fit with a Rayleigh distribution

$$P(r', w) = \frac{r'}{w^2} \exp\left(-\frac{(r')^2}{2w^2}\right)$$

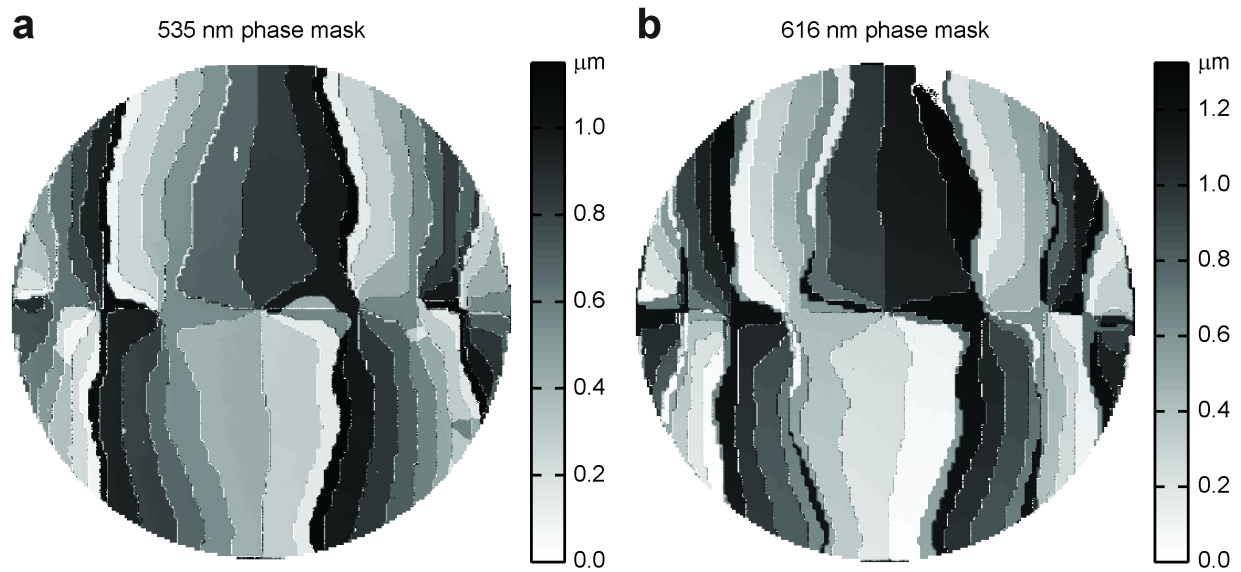
where $r' = \sqrt{(x')^2 + (y')^2}$ is the Euclidean distance to the helical fit and w represents the apparent width of the fiber. The good fit using this function shows that the distribution of points is well-approximated by a Gaussian distribution in y and z centered on the helix fit.

12 PopZ Volume Estimation

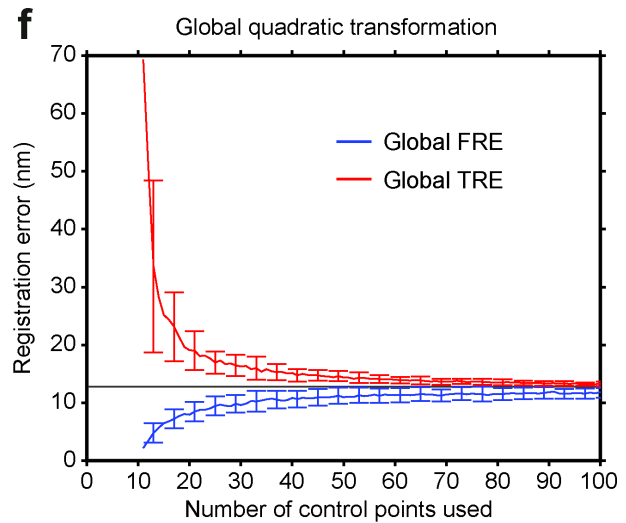
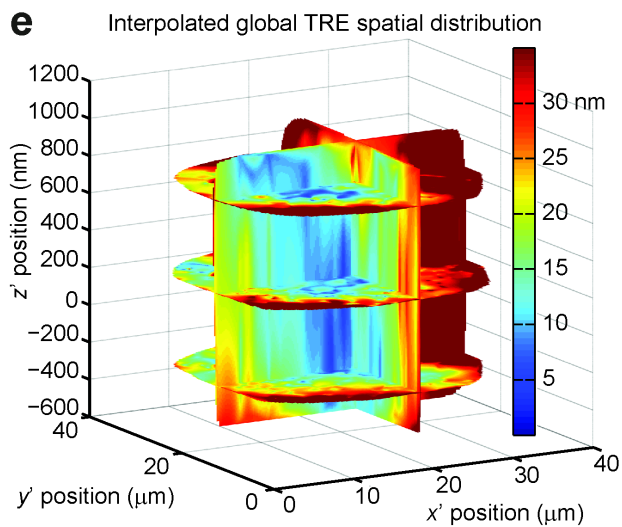
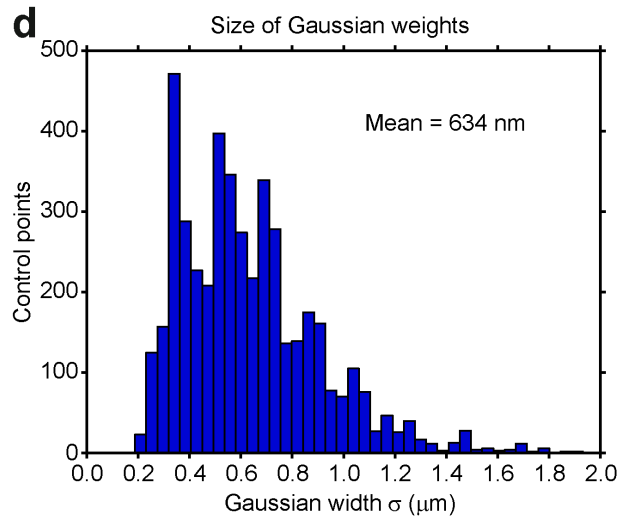
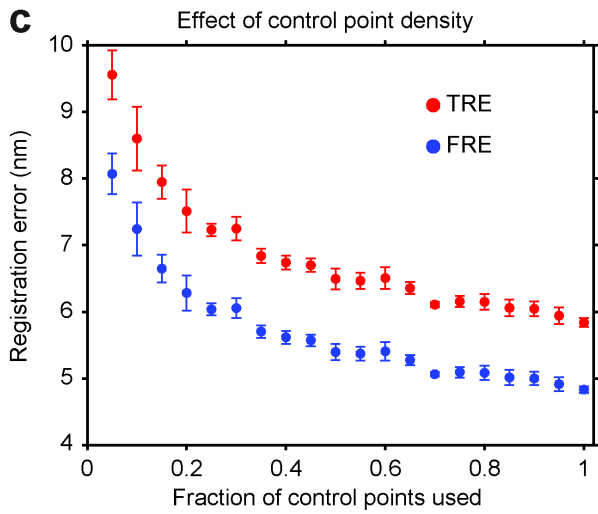
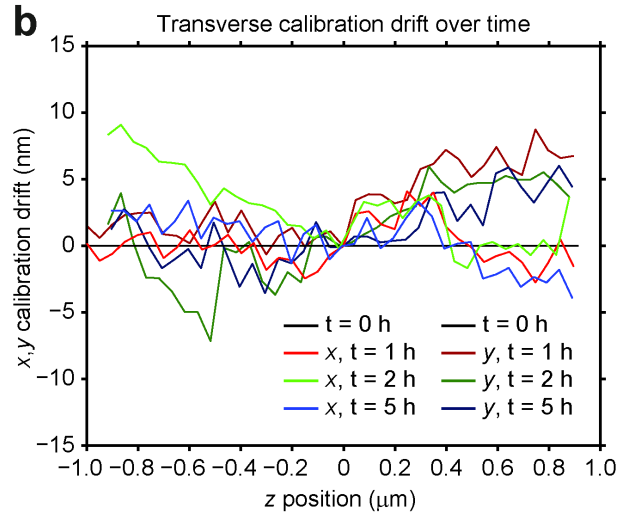
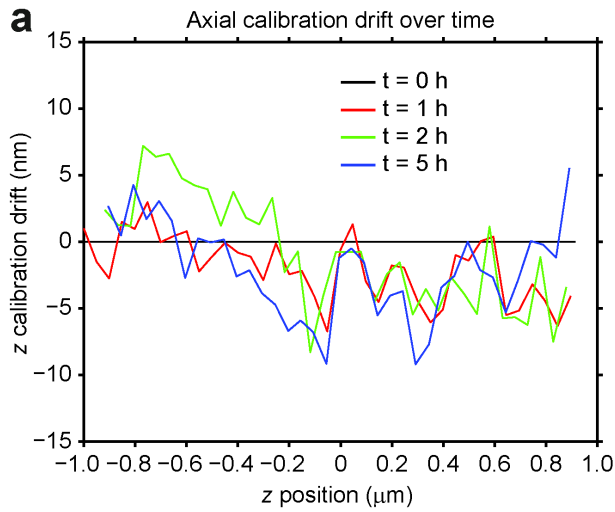
For each of the PopZ clusters, the single-molecule localizations were binned in a three-dimensional histogram with $32 \times 32 \times 32$ nm voxels. (The size of the voxels was chosen to be close to the median PAmCherry1-PopZ localization precision of $(\sigma_x, \sigma_y, \sigma_z) = (24.7, 25.7, 38.1)$ nm) For volume estimation, first the connectedness of the filled voxels in the 3D histogram was determined using the MATLAB built-in function `bwconncomp` with a 26-

point neighborhood connectivity criterion. This returned one large connected region of filled voxels and a few separated voxel regions which contained isolated localizations. The isolated localizations were considered to be out of the PopZ cluster and not included in the volume estimation. Within the large connected region some voxels were left unfilled due to the stochastic nature of the sampling process and the finite labeling density. By scanning through x , y , and z slices of the 3D histogram, we identified those empty voxels and labeled them as filled if, for each, at least 3 out of 4 surrounding neighbors were filled. This process was repeated until the number of filled voxels did not change any more (Supplementary Figure 4cd). This led to complete filling of the volume and giving it a more continuous shape. The PopZ nanodomain volumes were then computed by summing the volumes of all filled voxels. To avoid any bias originating from the initial placement of the voxel grid relative to the PAmCherry1-PopZ localizations, we shifted the grid in steps of 2 nm in x , y , and z and obtained volume estimates in each case. The mean values and the standard deviations of the resulting distributions were taken, respectively, as the final PopZ nanodomain volume estimates and the associated errors.

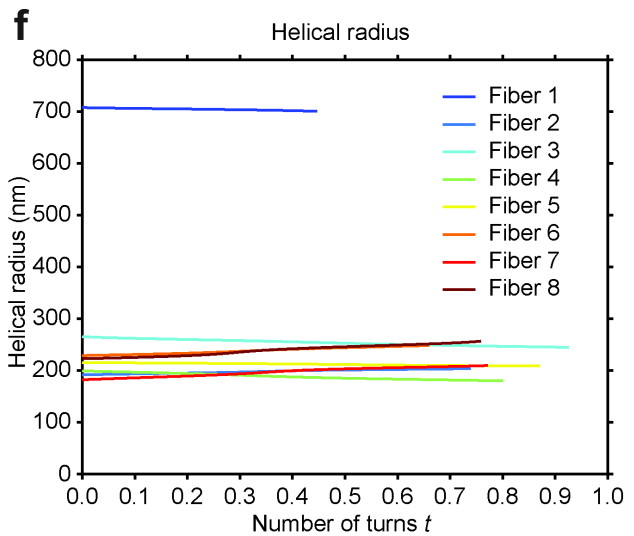
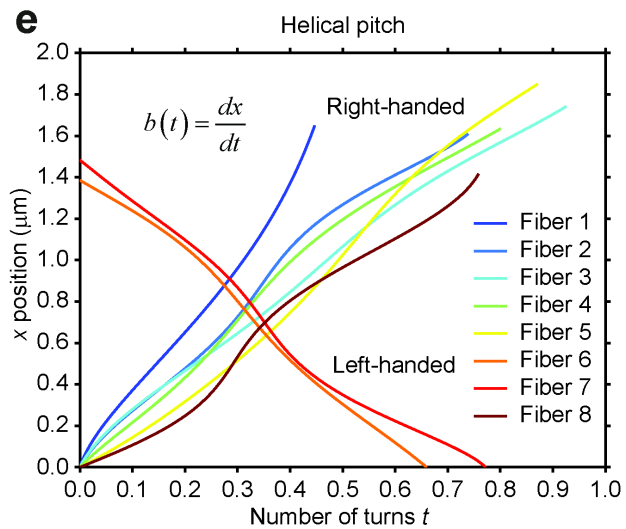
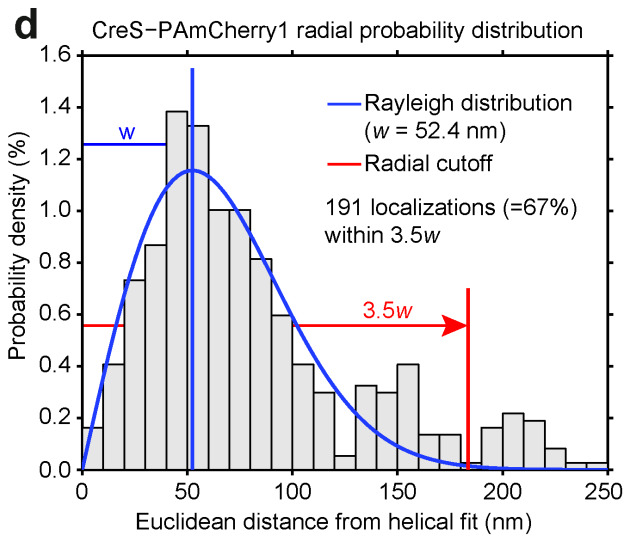
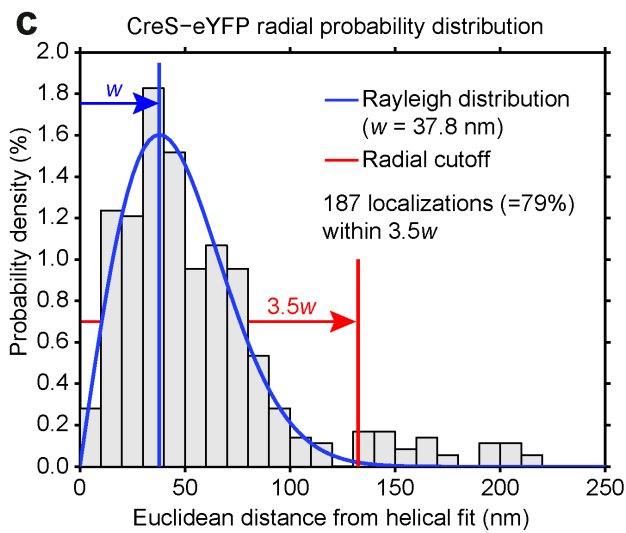
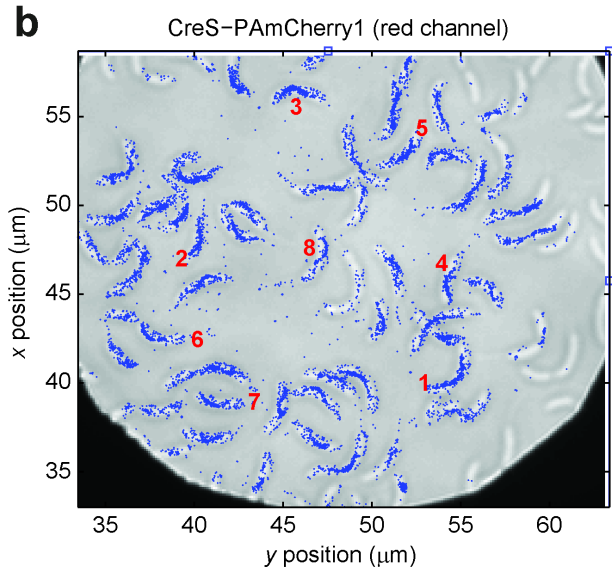
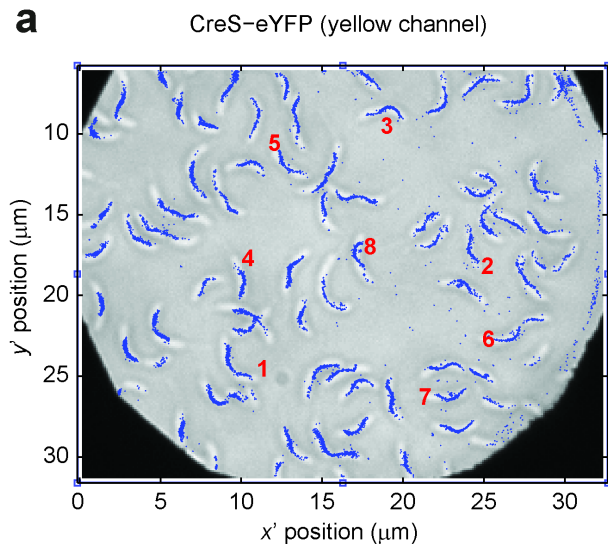
13 Supplementary Figures



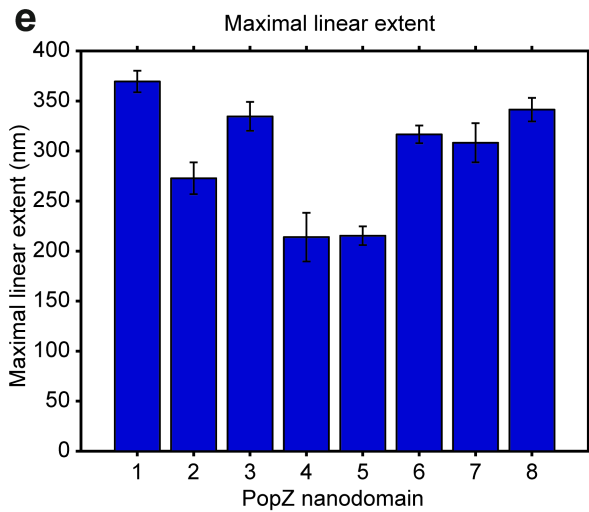
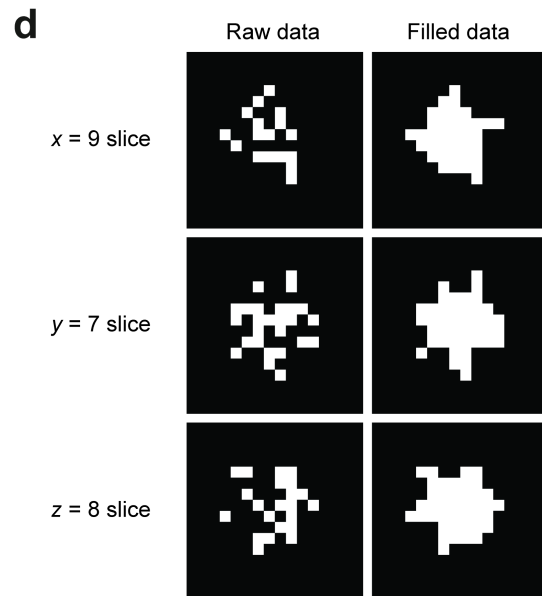
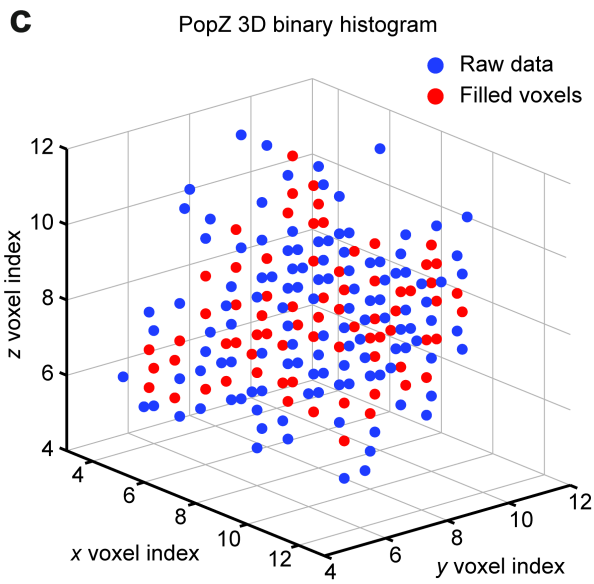
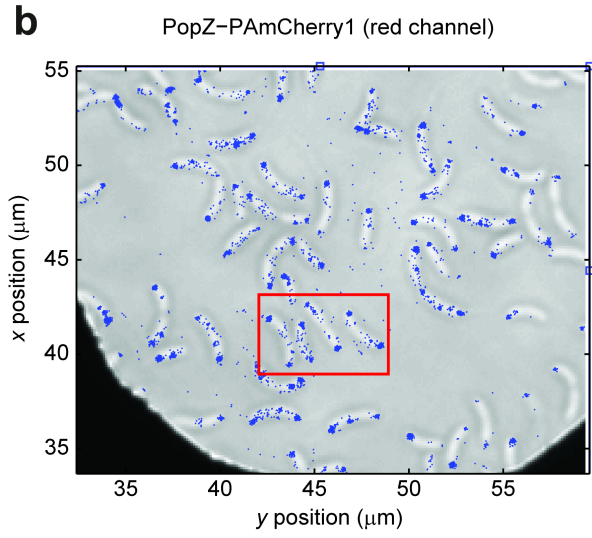
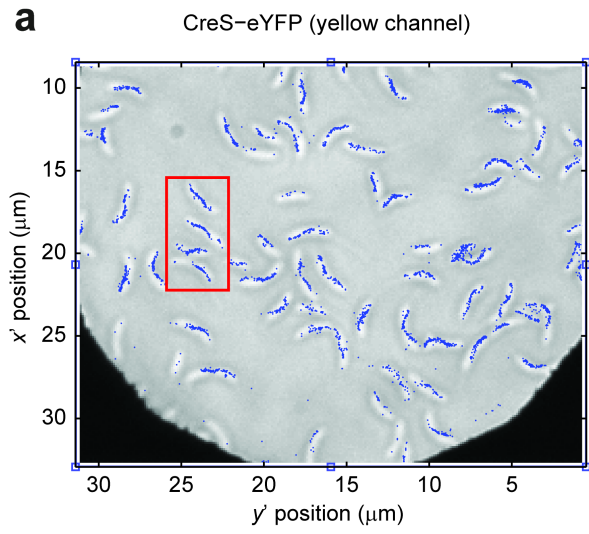
Supplementary Figure 1 DH-PSF phase masks **a** and **b** Measured profilometer scans of the quantized 8-level surface relief phase masks and optimized for the spectrally averaged mean emission wavelength in the two channels (616 nm and 535 nm, respectively, see Figure 1c). The colormaps show the height in microns.



Supplementary Figure 2 Contributors to non-zero registration errors and comparison to a global registration algorithm. **a** Temporal drift in the z fiducial calibration (see **Fiducial calibration**). Due to nanoscale movement of the optical elements in the imaging path, the DH-PSF instrumental response function can shift slightly and contribute to the measured registration errors. **b** Temporal drift in the corresponding x,y fiducial calibration. **c** The magnitude of the registration errors scale with the density of control points. Shown are the registration errors (mean \pm s.d., $n = 6$ measurements) calculated from a random fraction of the original set of control points. **d** Spatial size of Gaussian weights computed for the control points shown in Figure 3. **e** Global interpolated TRE, based on 17 randomly chosen control points. The performance of the global transformation is notably worse than the locally-weighted transformation, shown in Figure 3d. **f** Monte Carlo simulation to assess the performance of a global quadratic transformation function. For a small number of control points a close to exact global FRE will be obtained, but the performance throughout the rest of the image domain is significantly worse. Depending on the locations of the randomly chosen control points the global TRE may vary drastically, as evidenced by the larger error bars (\pm s.d., $n = 100$ iterations). Even as the number of control points is increased a global transformation cannot achieve the performance of a locally-weighted transformation. The global TRE eventually reaches the asymptote at 12.77 nm.



Supplementary Figure 3 Morphological measurements on CreS fibers in live *Caulobacter* cells. **a** and **b** Projected CreS-eYFP and CreS-PAmCherry1 localizations overlaid on the WL image in the yellow and red channel, respectively. Corresponding cells/fibers are numbered. **c** Radial CreS-eYFP probability distribution of fiber 2. We classified localizations that were a distance $>3.5w$ (116.4 nm) from the helical fit as cytosolic localizations. **d** Radial CreS-PAmCherry1 distribution of fiber 2. We classified localizations that were a distance $>3.5w$ (183.4 nm) from the helical fit as cytosolic localizations. **e** Comparison of the helical pitch of eight fibers computed from the pooled CreS-eYFP/ CreS-PAmCherry1 datasets. A majority of the helices are right-handed. **f** Comparison of the radii of curvature of eight fibers computed from the pooled CreS-eYFP/CreS-PAmCherry1 datasets. Fiber 1 displays a notable deviation from the frequently observed helical curling behavior.



Supplementary Figure 4 PopZ volume estimations in live *Caulobacter* cells. **a** and **b** Projected CreS-eYFP and PAmCherry1-PopZ localizations overlaid on the WL image in the yellow and red channel, respectively. The 4 cells shown in Figure 4c are outlined. **c** PAmCherry1-PopZ localizations at the cell poles were binned into 3D binary histograms (shown here is nanodomain 8). Unfilled voxels in the interior of the nanodomain volumes (red) were filled during post-processing. **d** Orthogonal slices through the 3D binary histogram shown in **c** before and after filling. **e** The maximal linear extent of the PopZ nanodomains is measured as the maximal Euclidian distance between filled voxels. This measurement is not affected by the filling process.

14 Supplementary Online Videos

Movie 1: Illustration of the mapping function used for image registration. Using a regular grid in x,y,z space (left), the mapping to x',y' , and z' is shown on the right. The distorted grid shows the relative aberrations between the two color channels.

Movie 2: Animated 3D rendering of the data in Figure 4a.

Movie 3: Animated 3D rendering of the data in Figure 4c.

Movie 4: Animated 3D rendering of the data in Figure 4d.

Supplementary Table 1 Fitted coefficients used in Equation 1.

Dimension	a	b
<i>x</i>	360000	22
<i>y</i>	350000	28
<i>z</i>	840000	23

15 References

36. Pavani, S. R. P.; Piestun, R. *Opt. Express* **2008**, *5*, 3484-3489.
37. Spektor, B. I. *Avtometriya* **1985**, *6*, 34-38.
38. Swanson, G. J. *MIT Lincoln Laboratory* **1989**, *Technical Report 854*, 1-47.
39. *Micro-optics : elements, systems and applications*; Taylor & Francis: London, 1997
40. Goshtasby, A. A. *Advances in Computer Vision and Pattern Recognition*; Springer Verlag: London, 2012
41. Thanbichler, M.; Iniesta, A. A.; Shapiro, L. *Nucleic Acids Res.* **2007**, *20*, e137.
42. Aqvist, J. *Comput. Chem.* **1986**, *2*, 97-99.
43. Lehmann, M.; Rocha, S.; Mangeat, B.; Blanchet, F.; Uji-i, H.; Hofkens, J.; Piguet, V. *Plos Pathogens* **2011**, *12*, e1002456.
44. Pertsinidis, A.; Zhang, Y.; Chu, S. *Nature* **2010**, *7306*, 647-651.